Prediction of the Fatigue Life of Cast Steel Containing Shrinkage Porosity

RICHARD A. HARDIN and CHRISTOPH BECKERMANN

A simulation methodology for predicting the fatigue life of cast steel components with shrinkage porosity is developed and validated through comparison with previously performed measurements. A X-ray tomography technique is used to reconstruct the porosity distribution in 25 test specimens with average porosities ranging from 8 to 21 pct. The porosity field is imported into finite element analysis (FEA) software to determine the complex stress field resulting from the porosity. In the stress simulation, the elastic mechanical properties are made a function of the local porosity volume fraction. A multiaxial strain-life simulation is then performed to determine the fatigue life. An adaptive subgrid model is developed to reduce the dependence of the fatigue life predictions on the numerical mesh chosen and to account for the effects of porosity that is too small to be resolved in the simulations. The subgrid model employs a spatially variable fatigue notch factor that is dependent on the local pore radius relative to the finite element node spacing. A probabilistic pore size distribution model is used to estimate the radius of the largest pore as a function of the local pore volume fraction. It is found that, with the adaptive subgrid model and the addition of a uniform background microporosity field with a maximum pore radius of 100 μm, the measured and predicted fatigue lives for nearly all 25 test specimens fall within one decade. Because the fatigue lives of the specimens vary by more than four orders of magnitude for the same nominal stress amplitude and for similar average porosity fractions, the results demonstrate the importance of taking into account in the simulations the distribution of the porosity in the specimens.

I. INTRODUCTION

INHOMOGENEITIES due to porosity are currently not considered in the design of structural components made from metal castings. Instead, *ad hoc* safety factors are used to address a designer's uncertainty in how the casting will perform in service. These safety factors are based on the assumption that castings perform unpredictably, if not poorly. Applying such safety factors to the entire cast material might do little for the robustness of the design other than increase the casting weight. Many part designers become frustrated by castings designed with very large safety factors that fail in service; they are hesitant to use castings. Such frustrations could be avoided if the quality of the cast metal throughout the casting could be known ahead of time and incorporated into the design.

The present study extends our recently developed method of modeling the effects of porosity on stiffness and stress redistribution[1] to the prediction of the fatigue life of steel castings containing porosity. For ease of use in standard design practice, commonly used commercial software is employed in the present stress and fatigue life simulations. The part design can be made safe by assuring that the casting process results in the best possible quality (*i.e.*, lowest porosity) steel at highly stressed locations. Should porosity form, the casting rigging or process parameters can be changed so that the porosity will not affect the service performance of the part. If designers wish to use lighter-weight and more thinly walled steel castings, understanding the effects of porosity becomes especially critical. An integrated design process is emerging in which a casting process simulation that predicts the location, amount, and size of the porosity is directly coupled with the mechanical simulation of the part performance that takes into account the effects of porosity.[2] It is anticipated that such a design process will also help guide and improve casting inspection procedures, by linking acceptance criteria with expected performance.

Fatigue life analysis can be divided into two parts:[3] (1) the stage of life of the component up to the initiation of a crack on the order of 1 mm in size and (2) the stage of life of the component undergoing the growth of a crack and its propagation to failure. The combination of the two gives the total life of a component. Perhaps the most often used approach to predicting crack initiation is the strain-life method,[3–6] in which specimen fatigue life test data to failure is fitted to the strain-life curve and the curve is used in life estimation. Because fatigue test specimens are small compared to most components, once cracks initiate in them, propagation is very rapid. The total life from the strain-life testing of specimens is

RICHARD A. HARDIN, Research Engineer, and CHRISTOPH BECKERMANN, Professor, are with the Department of Mechanical and Industrial Engineering, University of Iowa, Iowa City, IA 52242. Contact e-mail: becker@engineering.uiowa.edu

the crack initiation life, because the second stage of life is extremely short relative to the first, for these test conditions. Multiaxial strain-life models[7–12] have been implemented in commercial software packages (fe-safe, for example[13]), to predict the durability of components from finite element analyses (FEAs). The second stage of fatigue life, the "fatigue crack growth" stage, is described using fracture mechanics, in particular, linear elastic fracture mechanics (LEFM), in which crack growth is assumed to follow the Paris–Erdogan equation.[14] Here, a crack pre-exists, formed either from fatigue crack initiation or during manufacturing of the part; the crack growth is determined by the stress field and material properties until failure.[3,14] Because the largest possible nonpropagating crack can be predicted for a given material and an alternating stress field using fracture mechanics, it can be used in damage-tolerant design life prediction in castings.[15–17]

The effects of porosity on the fatigue behavior of cast metals have been measured in steels,[18–24] in cast irons,[16,17,25,26] and in aluminum alloys.[27–36] Also, Murakami[37] gives a good overview of the effects of small defects and inclusions on metal fatigue. Jayet-Gendrot et al.[20] have reviewed the fatigue and fracture literature for steel and other metals and showed that the fatigue behavior depends on the pore size and volume fraction. For example, in stainless steel, they report that reductions in fatigue strength of 35 and 50 pct are observed for areas of crack initiating defects of less than and greater than 3 mm^2, respectively, in a specimen test section 70 × 22 mm in size.[21] Based on the square root of the defect area as a representation of the dimension of the porosity,[37] this size is approximately 55 μm. Also, for low-alloy steel, fatigue strength reductions from 8 to 30 pct were reported when shrinkage porosity cavities covered 3 to 7 pct of the fracture surface.[22] Recently, for an aluminum alloy, Linder et al.[29] measured a 15 pct decrease in fatigue strength for smooth specimens when the porosity level was increased from 0.7 to 4.1 pct, while notched specimens gave no dependence on porosity in the same range. Extreme value statistics[28–30,34,37] have been used to show the strong dependency of fatigue life on the maximum likely pore size from measured pore size distributions.

Crack initiation life analyses of cast components in the presence of porosity have been performed by using the strain-life approach and modeling the pores as equivalent notches.[18–24,26,31–33] Applying a strain-life model alone assumes that crack nucleation encompasses the majority of the life of the component and that the time for fatigue crack propagation to fracture is insignificant relative to crack initiation. The use of strain-life models requires that pore geometry information, primarily the minimum notch radius and the major axes of the ellipsoidal notch, be known or be determined from fracture surfaces, to determine a stress concentration factor. Researchers studying aluminum castings have treated pores in castings as notches for predicting the effect of porosity on crack initiation life[31] and the mechanism of crack formation and growth from pores.[33] For the second stage of component life, fatigue life estimation of cast metals by fracture

mechanics approaches are used: for nodular cast iron,[16,17,25,26] cast aluminum alloys,[27,32–36,38] and steel alloys.[15,19,20,23] One difficulty in applying fracture mechanics concepts to cast parts is determining the final, or failure, crack length. For example, failure of components has been assumed when the remaining net section area stress is at or is greater than the yield strength[19] and when the crack depth propagates to the section wall thickness at the defect location.[15] A comparison between the measured fatigue life of cast steel test specimens containing porosity and inclusions and the fatigue life obtained by modeling the specimen using crack initiation (local stain-life concepts) and LEFM approaches has been presented.[23] In the crack initiation model, the defects were considered to be three-dimensional notches; in the crack growth model, the defects were treated as two-dimensional elliptical cracks having an envelope around the defect. It was found[23] that the crack initiation estimate of life was more accurate than the fracture mechanics approach, and that interpreting the porosity as pre-existing cracks resulted in too conservative an estimate of the fatigue life. Dabayeh and Topper[32] came to a somewhat different conclusion for cast aluminum, in which the local strain approach gave quite nonconservative estimates of fatigue life and the crack growth method gave better agreement. The current authors have found that local strain-life modeling of porosity as a notch gave better agreement with measurements than did LEFM in cast 8630 steel.[19]

In the present study, a simulation method is developed to predict the measured fatigue lives of 25 cast steel specimens containing up to 21 pct shrinkage porosity over the gage length. This is a challenging task, not only because the measured fatigue lives of the specimens are much below the values corresponding to sound steel, but also because the measured lives vary by more than four orders of magnitude at the same applied stress amplitude.[19] These variations can only be attributed to the different amounts and distributions of porosity within the specimens. The fatigue tests and the tomographic reconstruction of the porosity fields in the specimens[1] are briefly reviewed in Section II. In Section III, the procedures and results of the fatigue life simulations are presented. An FEA is performed to determine the complex stress field resulting from the porosity;[1] multiaxial strain-life analysis is used to compute the fatigue life distribution in the specimens. The strain-life approach is adopted here, because the preliminary calculations in Reference 19 revealed that LEFM does not predict the measured fatigue lives of the specimens. An adaptive subgrid fatigue notch factor model, which approximately accounts for the effect of porosity that is under-resolved by the computational mesh used in the stress and fatigue life simulations, is presented in Section IV. As part of this subgrid model, a probabilistic pore size distribution model for determining the maximum pore radius as a function of the local pore volume fraction is developed. Detailed comparisons are made between the measured and predicted fatigue lives. The conclusions of the present study are summarized in Section V.

II. EXPERIMENTS

Fatigue tests were performed using cast and heat treated AISI 8630 steel specimens containing a range of shrinkage porosity. All the details of these experiments, together with the results of fractography and preliminary fatigue life calculations, were presented in Reference 19. Prior to the fatigue testing, X-ray tomography was performed on the machined specimens, in order to obtain a measured three-dimensional porosity field within each specimen. The details of the tomographic reconstruction procedures were recently presented in Reference 1. For completeness, a brief overview of these tests and measurements is provided here.

A. Cast Specimens

Specimen blanks were cast from AISI 8630 steel. The mold geometry was designed using computer modeling, to obtain a range of shrinkage porosity levels.[19] The cast blanks were 152-mm-long cylinders having a nominal 14.3 mm diameter. To produce shrinkage porosity, a cylindrical disk 25.5 mm in diameter was positioned at the midlength of the blanks, as shown in Figure 1. This design concentrated the porosity at the centerline and midlength of the cast blanks, so that the porosity could be located in the gage section of the test specimens. The severity of the porosity was controlled by varying the disk thickness (dimension along the casting length); disk thicknesses of 5, 7.5, and 10 mm were cast. Generally, a smaller disk thickness resulted in
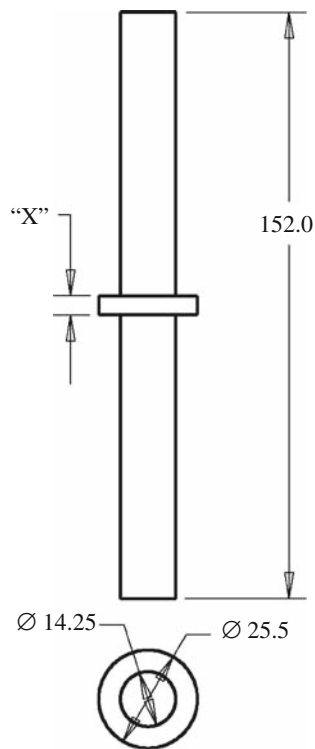
a lower porosity level, but there was overlap of the porosity levels among the three disk thickness groups. Cut surfaces of specimens from castings having disk thicknesses of 5, 7.5, and 10 mm are shown in Figures 2(a), (b), and (c), respectively. It can be seen that the porosity level ranges from dispersed macroporosity to holes and gross section loss. Radiographs are shown to the right of each cut specimen surface with a

Fig. 1—Dimensions of cast porous specimen blanks in millimeters. Dimension "X" = 5, 7.5, and 10 mm for the "least," "middle," and "most" porosity specimen groups, respectively.
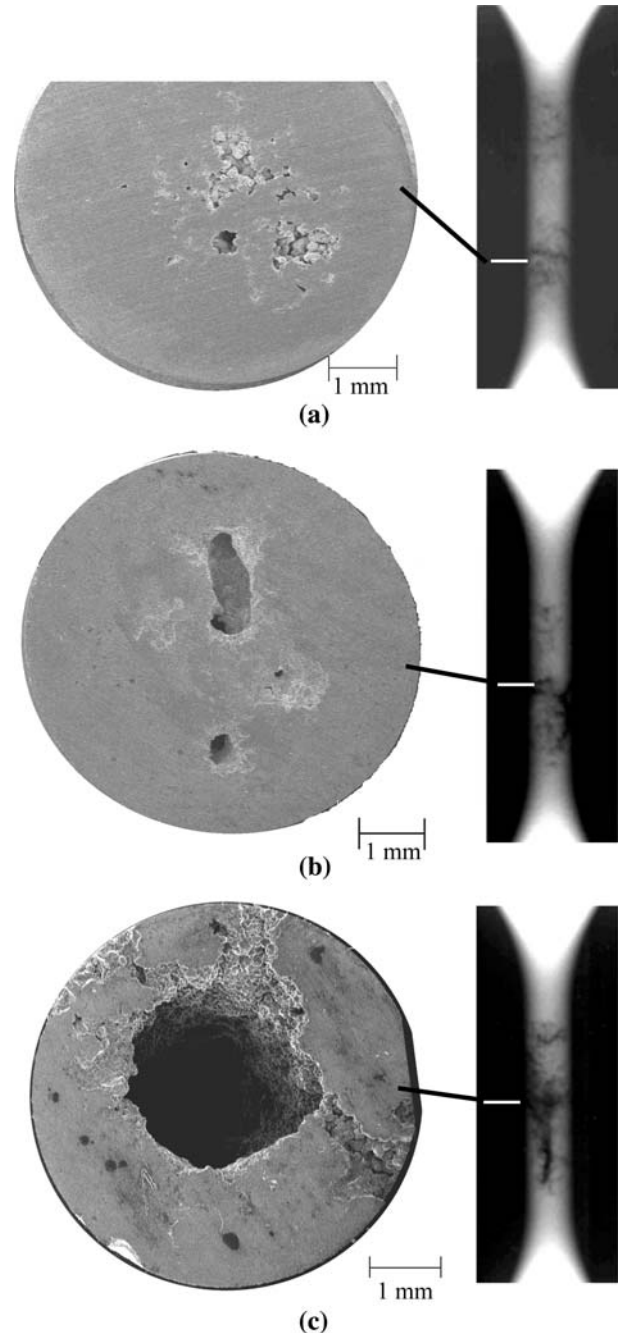

Fig. 2—Cut and polished surfaces of three specimens cast with different porosity levels ranging from (a) specimen 22 representing the least, to (b) specimen 3 representing the middle range, to (c) specimen 13 representing the most porosity. Radiographs of the specimen gage sections are given to the right of each surface, with the longitudinal position of the cut indicated.
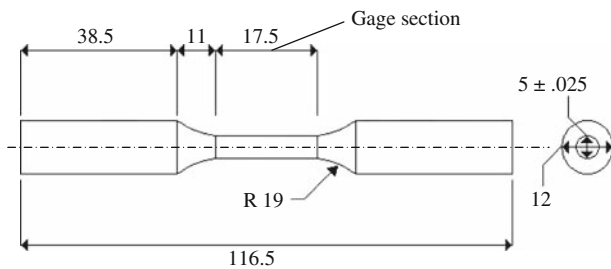
Fig. 3—Dimensions of test specimens in millimeters.

white mark that indicates the approximate location of the cut along the length of the machined specimen. Comparing these radiographs qualitatively, the porosity appears to be increasingly severe proceeding from Figure 2(a) to Figure 2(b), and to Figure 2(c). In some specimens, as shown, for example, in Figure 2(c), porosity extended to the specimen surface.

The cast blanks received identical heat treatment: they were normalized at 900 °C, austenized at 885 °C, water quenched, and finally tempered for 1 1/2 hours at 510 °C. This heat treatment resulted in a tempered martensitic structure with a Rockwell C hardness of 34. The blanks were then machined to the dimensions shown in Figure 3. More than 50 specimens were produced in this manner.[19]

B. Tomography for Porosity Measurement

The X-ray tomography of the machined specimens was performed in order to obtain a measured three-dimensional porosity field within each specimen. This method is described in detail in Reference 1. In brief, film radiography of the specimens was performed using a sensitivity of 2 pct of the gage section diameter, which corresponds to a resolution of approximately 100 μm. Three examples of radiographs are shown in Figure 2. Orthogonal radiographic views of each specimen were obtained. The radiographic films were digitized using an X-ray scanner resulting in 8 bit gray level, 1200 dpi (~21 μm pixel side length) images. The gray level information was converted to porosity percentage using an *in-situ* calibration method. A tomography algorithm[1,39] was then employed to reconstruct a three-dimensional porosity field from the orthogonal views. Figure 4 shows two examples of porosity fields obtained in this manner. The X-ray tomography technique used cannot resolve the exact geometry of the shrinkage pores on a microscopic scale. This would require a resolution on the order of 1 μm over a specimen gage length and diameter of 17.5 and 5 mm, respectively, which is not possible given present day computing resources. The porosity volume fractions obtained in the tomographic reconstruction correspond to voxels that have a side length of ~21 μm. If a voxel falls entirely within a pore (or sound steel), the porosity volume fraction is equal to unity (or zero). In the simulations presented here, the measured porosity fields are mapped onto computational meshes with node spacings that are one to two orders of magnitude larger

than the voxel side length, *i.e.*, between 100 μm and 1 mm. Thus, the accuracy and resolution of the present tomographic reconstruction technique were deemed to be sufficient (also Reference 1).

Table I lists the average porosity volume fraction measured for the 25 specimens for which a tomographic reconstruction was performed. The average porosity fractions listed in the table correspond to a 12 mm long center portion of the gage section, rather than the entire 17.5 mm gage length (Figure 3) over which the porosity field was reconstructed; this is related to the location of the extensometer with which the strain was measured (Section C). It can be seen that the average porosity varies from approximately 8 to 21 pct. Table I also lists the maximum cross-sectional porosity fraction for each specimen. This fraction was obtained by averaging the porosity over one voxel thick cross-sectional slices and selecting the maximum value along the gage length. It varies from approximately 15 to 59 pct. It is shown in Reference 1 that this maximum cross-sectional porosity, rather than the average volume fraction over the gage length, correlates well with the measured effective elastic modulus, *E*, of the specimens.

C. Fatigue Testing

The specimen preparation and fatigue testing were carried out according to the ASTM E606 standard.[4] All fatigue tests were performed under fully reversed, $R = -1$, loading conditions. During fatigue testing, the mechanical behavior of the specimens was found to be elastic; therefore, load-controlled testing at 10 to 20 Hz was used. This permitted accurate strain amplitude measurements while using the faster testing capability of load control. All fatigue tests were performed until fracture of the specimen occurred or a runout life was achieved at 5×10^6 cycles. Four nominal stress amplitudes, $\Delta S/2$, were applied and held constant during testing of the specimens: 126, 96, 66, and 53 MPa; these stress levels were selected to obtain a large range of measured fatigue lives while avoiding runouts. An extensometer with ends at 6 mm above and below the midpoint of the specimen length was used to measure the strain amplitude. The effective (or apparent) elastic modulus *E* was determined from the measured strain and load data, using the "sound" specimen gage cross-sectional area to determine the nominal stress. The measured elastic moduli and fatigue lives of the 25 specimens for which the measured fatigue live was less than the runout life are given in Table I; reference will be made to individual specimens in the table using the specimen numbers.

The monotonic and cyclic material properties for sound 8630 steel were measured in Reference 40 and are provided in Tables II and III, respectively. The cyclic stress-strain curve is given by

$$\frac{\Delta e}{2} = \frac{\Delta S}{2E} + \left(\frac{\Delta S}{2K'}\right)^{\frac{1}{n'}} \quad [1]$$

where $\Delta S/2$ and $\Delta e/2$ are the nominal stress and strain amplitudes, respectively; K' is the cyclic strength
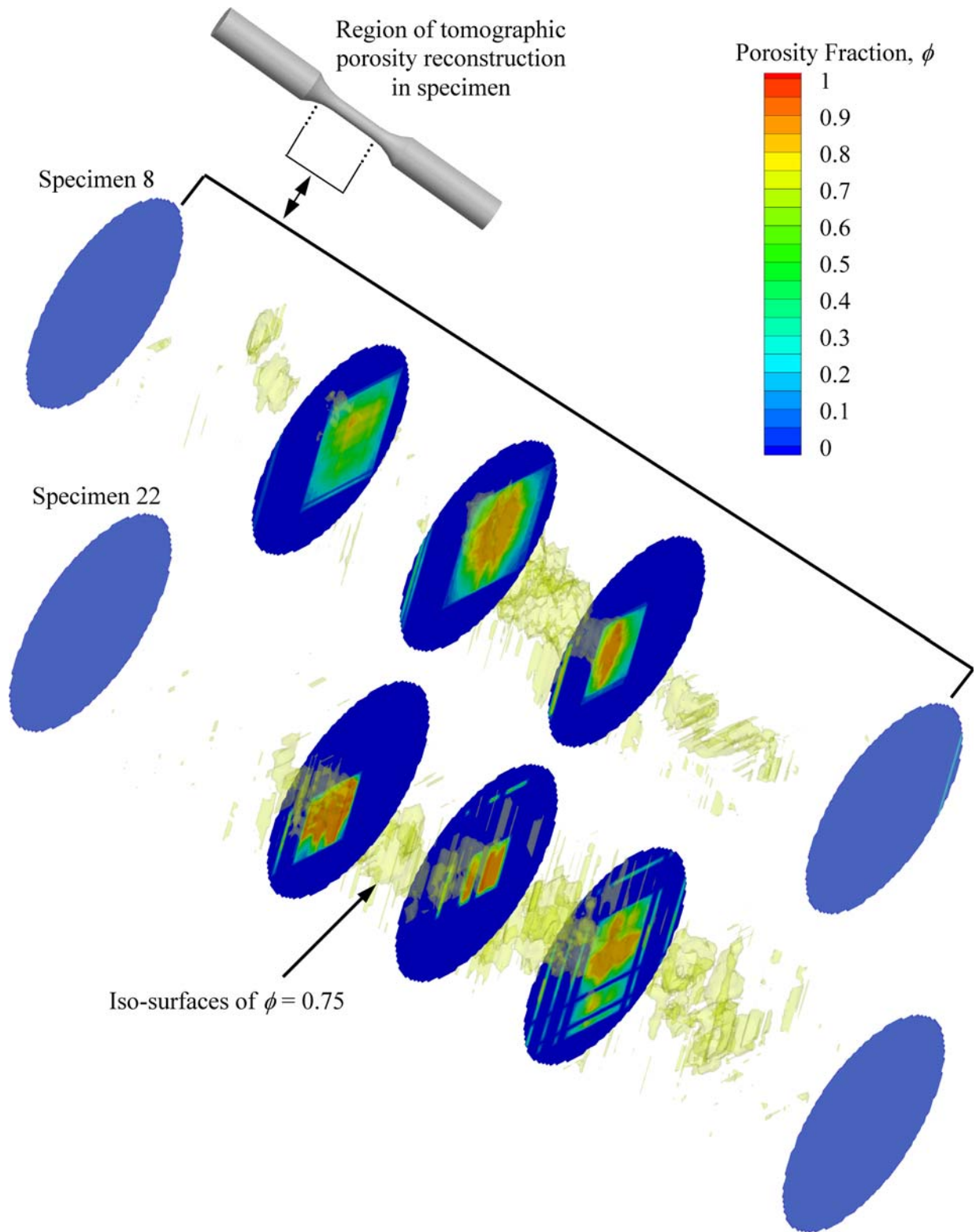
Fig. 4—Example of internal porosity distributions reconstructed from X-ray tomography in the test section of fatigue test specimens 8 and 22. Slices at three axial positions are shown for each specimen.

coefficient; and n' is the cyclic strain hardening exponent. Note from Tables II and III that the 661 MPa value for the cyclic yield strength, S'_y, is much less than the monotonic yield strength, S_y, value of 985 MPa, indicating the presence of considerable cyclic softening. The strain-life curve (often referred to

Table I. Summary of Measurements for 25 Cast Steel Specimens Containing Porosity:[1,19] Test Stress Level, Porosity from Radiographic Analysis, Strain, Elastic Modulus, and Fatigue Life

Specimen Number	Applied Stress Level of Test (MPa)	Average Porosity Volume Fraction in Gage Section	Maximum Cross-Sectional Porosity Fraction	Strain $\times 10^4$	Elastic Modulus (GPa)	Fatigue Life (Cycles)
1	96	0.104	0.432	7.01	137	1365
2	96	0.101	0.208	6.44	149	79,908
3	126	0.101	0.256	8.81	143	24,320
4	53	0.128	0.297	3.84	138	851,275
5	126	0.097	0.185	8.24	153	29,023
6	66	0.134	0.275	4.55	145	216,516
7	66	0.095	0.201	4.68	141	4,053,800
8	66	0.185	0.363	4.89	135	57,566
9	53	0.146	0.587	6.09	87	10,812
10	126	0.213	0.326	9.33	135	37,089
11	66	0.117	0.250	4.85	136	113,503
12	66	0.148	0.415	5.84	113	15,419
13	96	0.185	0.538	12.47	77	6042
14	126	0.139	0.507	10.50	120	160
15	53	0.187	0.551	6.09	87	15,868
16	66	0.076	0.160	3.98	166	1,681,018
17	96	0.096	0.254	8.65	111	4392
18	53	0.085	0.148	3.66	145	1,342,218
19	126	0.093	0.225	8.87	142	13,013
20	53	0.099	0.182	3.71	143	249,752
21	96	0.122	0.300	7.68	125	41,066
22	66	0.117	0.262	4.37	151	769,074
23	126	0.121	0.205	8.13	155	40,896
24	96	0.144	0.288	6.76	142	333,025
25	126	0.129	0.280	8.51	148	7456

Table II. 8630 Steel Monotonic Properties[40]

Property	Sound Material
S_u (MPa)	1,144
S_y (MPa)	985
E_0 (GPa)	207
Pct EL	not measured
Pct RA	29
σ_f (MPa)	1,268
ε_f (MPa)	0.35
K (MPa)	not measured
N	not measured

Note: EL = elongation, RA = reduction in area.

Table III. 8630 Steel Cyclic Properties[40]

Property	Sound Material
S_f (MPa)	293
S_f/S_u	0.26
K' (MPa)	2,267
n'	0.195
S_y' (MPa)	661
b	−0.121
c	−0.693
σ_f' (MPa)	1,936
ε_f'	0.42

as the Coffin–Manson relationship[5,6]) for sound 8630 steel is given by

$$\frac{\Delta\varepsilon}{2} = \frac{\Delta\varepsilon_e}{2} + \frac{\Delta\varepsilon_p}{2} = \frac{\sigma_f'}{E}(2N_f)^b + \varepsilon_f'(2N_f)^c \quad [2]$$

where $\Delta\varepsilon/2$, $\Delta\varepsilon_e/2$, and $\Delta\varepsilon_p/2$ are the total, elastic, and plastic strain amplitudes, respectively; $2N_f$ is the number of reversals to failure; σ_f' is the fatigue strength coefficient; b is the fatigue strength exponent; ε_f' is the fatigue ductility coefficient; and c is the fatigue ductility exponent. The sound 8630 steel cyclic properties listed in Table III were obtained in Reference 40 by fitting test data to Eqs. [1] and [2]. For sound 8630 steel, the fatigue strength (or fatigue limit), S_f, at 5×10^6 cycles is equal to 293 MPa.

The measured fatigue lives (as cycles to failure, N_f) of the porous specimens are plotted in Figure 5 as a function of the applied stress amplitude, $\Delta S/2$. In Figure 5(a), the measurements are compared to the stress-life curve for sound 8630 steel. The sound stress-life curve was obtained from Eq. [2] by converting the strain to stress using the elastic modulus from Table II; plasticity was found to be negligibly small.[19] It can be seen that the fatigue lives of the porous specimens fall far below the sound material curve. Depending on the number of cycles to failure, the stress amplitudes in the present tests are between approximately 170 and 900 MPa below the stress amplitudes for sound 8630
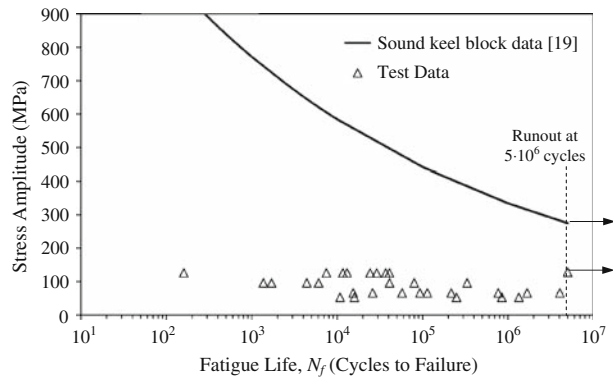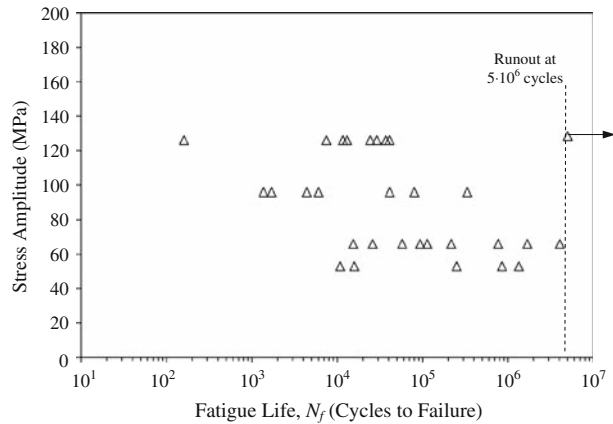
Fig. 5—(a) Fatigue life measurements of specimens with porosity compared with sound data from Ref. 40. (b) Measured fatigue lives of specimens with porosity tested at four stress levels: 126, 96, 66, and 53 MPa. Note the single runout specimen.

steel. If the specimens had been sound, they would all have a life greater than the runout value ($>5 \times 10^6$ cycles). The porous specimen data is examined in more detail in Figure 5(b). For all applied stress levels, large variations in the measured fatigue lives can be observed. The lives of the porous specimens range from 160 cycles to a runout. Clearly, the fatigue behavior of these specimens is primarily controlled by porosity. However, the variation in the measured fatigue life of more than four orders of magnitude cannot be explained by the comparably small differences in the average porosity of the specimens (between 8 and 21 pct (Table I)). These results demonstrate that each specimen has a unique porosity field; this, in combination with the loading, results in a complex stress field that must be accurately simulated in order to predict the fatigue life of a given specimen.

III. FATIGUE LIFE PREDICTION

A. Simulation Procedure

The present procedure for predicting the fatigue life of the porous specimens can be summarized as follows.

(a) Map the measured porosity field from the tomography onto the nodes of the FEA mesh.

(b) Degrade the elastic properties at each node according to the local porosity fraction, ϕ.

(c) Perform a finite element elastic stress analysis that corresponds to the loading in the fatigue tests.

(d) Import the predicted stress fields corresponding to tension and compression into the life prediction software and perform a multiaxial strain-life analysis.

The first three steps in this procedure were developed previously by the present authors; all details can be found in Reference 1. In brief, the three-dimensional quadratic interpolation subroutine QD3VL from the International Mathematics and Statistics Library (IMSL)[41] is used to map the porosity data onto the FEA mesh. Ten-node quadratic tetrahedral elements are used to perform the stress analysis. Elastic mechanical properties are assigned at each node as a function of the porosity fraction at that location. The local elastic modulus is calculated from[1]

$$E(\phi) = E_0 \left(1 - \frac{\phi}{0.5} \right)^{2.5} \qquad [3]$$

where E_0 is the elastic modulus of the sound material and ϕ is the porosity volume fraction. The Poisson ratio, v, as a function of ϕ is obtained from a relationship developed by Roberts and Garboczi:[42]

$$v(\phi) = v_S + \frac{\phi}{\phi_\infty}(v_\infty - v_S) \qquad [4]$$

with $v_\infty = 0.14$, $\phi_\infty = 0.472$, and $v_S = 0.3$. Significant plasticity was not detected during testing of the specimens; therefore, plastic effects are ignored in the FEA simulations.[19] Mechanical simulation of the specimens with porosity is performed using ten-node quadratic tetrahedral stress/displacement elements (type C3D10) with the commercial FEA package Abaqus/Standard (version 6.6.1).[43] The FEA simulation boundary conditions are chosen to closely match the test conditions. During testing, the specimens were held fixed at their upper grip, and the loading was applied to the lower (ram) end, which was free to move vertically, placing the specimen in tension and compression during fatigue testing. The simulated specimen geometry considers only the initial 5 mm of the length of the grips in the FEA mesh. This is a distance away from the fillet and test section that is more than sufficient for producing stress-strain results that are insensitive to the locations at which the boundary and loading conditions are applied. Shorter execution times are the only difference from simulations using more of the grip length. At the upper grip face, a clamped boundary condition is applied (having no translations or rotations); at the lower grip, translations are allowed only in the axial direction, with no axial rotation allowed. A uniform distributed loading is applied over the face at the lower grip end, to produce the total load corresponding to the testing conditions. Using this procedure, it is shown in Reference 1 that the measured strains (Table I) are predicted to within approximately ±10 pct. This good agreement is achieved for an FEA node spacing of

0.25 mm, but the results are relatively independent of the mesh for node spacings up to 2 mm.[1] These results show that, by using porosity fractions that are defined over a volume that is small compared to the (macroscopic) specimen geometry but large compared to the (microscopic) pore geometry, and by degrading the elastic properties locally in accordance with the porosity fraction, the overall stiffness response of the specimens can be simulated accurately.

After running ABAQUS, the resulting stress fields corresponding to the tension and compression steps of the fully reversed loading ($R = -1$) are imported into the fatigue life prediction software. In the present study, the software package fe-safe[13] is used for the fatigue life calculations. The loading cycle and the fatigue properties for the sound material (Table III) are entered into the fe-safe model. The nodal stress tensors from the Abaqus simulations are converted to strains within the fe-safe software, using a sound material elastic modulus of 207 GPa (Table II). As long as this elastic modulus is used throughout the fatigue calculations, the use of a variable E is not necessary as the alternating strain amplitude and the elastic term in the strain-life equation scale with whatever modulus is used. In the present study, fe-safe's multiaxial Brown–Miller algorithm with the Morrow mean stress correction is used to calculate the fatigue life as cycles to failure. For steel, fe-safe recommends using the multiaxial Brown–Miller algorithm for ductile steel and the principle strain algorithm for brittle steels, both with the Morrow mean stress correction.[13] The Brown–Miller algorithm is said to be a more conservative method; it uses a critical plane analysis to determine the life in reversals to failure, $2N_f$, by solving

$$\frac{\Delta\gamma_{\max}}{2} + \frac{\Delta\varepsilon_n}{2} = 1.65\frac{(\sigma_f' - \sigma_m)}{E}(2N_f)^b + 1.75\varepsilon_f'(2N_f)^c \quad [5]$$

at each node, where $\Delta\gamma_{\max}/2$ is the maximum shear strain amplitude, $\Delta\varepsilon_n/2$ is the strain amplitude normal to the shear stress plane, and σ_m is the mean stress. The critical plane is defined as the plane having the maximum value of $\Delta\gamma_{\max}/2 + \Delta\varepsilon_n/2$. In the critical plane analysis, the calculated strain tensor at a finite element node (having three direct and three shear components) is resolved onto a number of planes where the damage associated with the strain is evaluated on each plane. The plane with the most damage is then selected for use in the strain-life calculations. In a Cartesian x-y-z coordinate system, unique planes can be defined by the orientation the normal of the plane surface makes with respect to the coordinate system. This orientation can be defined by one angle from the x-axis toward the y-axis, and a second angle from the z-axis toward the x-y plane.[13] The software fe-safe searches for the critical plane with the worst damage (shortest life) in 10 deg increments over the 180 deg range of the first angle and the 90 deg range of the second angle. Direction cosines are used to project the strains onto the calculation plane. Additional details about multiaxial fatigue analysis can be found in the book by Socie and Marquis.[7]

B. Results of Fatigue Life Simulations Using Multiaxial Strain-Life Method

Figure 6 shows a series of simulation results for specimen 19 on a longitudinal center section, starting with the measured porosity field mapped onto the FEA mesh and followed by the predicted maximum principle stress and strain fields and, finally, the predicted cycles to failure field. The latter is also shown on the surface of the specimen. In these baseline simulations, a node spacing of 0.25 mm is used. As mentioned previously, this grid of approximately 20 nodes across the specimen diameter was found to give good results for the overall stiffness.[1] It can be seen that the porosity causes a complex three-dimensional stress field to develop in the specimen during loading. Larger stresses are observed adjacent to regions with a high porosity fraction. On the other hand, large strains coincide with high porosity fractions. The shortest lives are predicted in regions of high stress concentration. For this specimen, the node
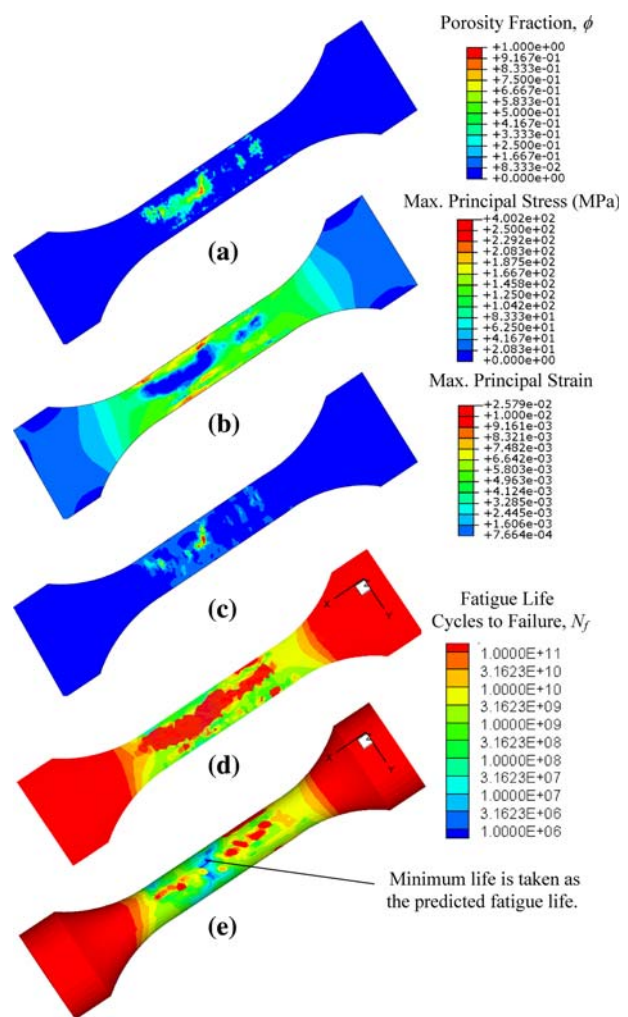

Fig. 6—Results in a longitudinal section for specimen 19. (a) Porosity distribution from tomography. Results from Abaqus stress analysis for (b) maximum principal stress and (c) maximum principal strain. Fatigue life prediction from fe-safe using Abaqus results (d) in the section and (e) on the surface with minimum predicted life of 15,847 cycles indicated.
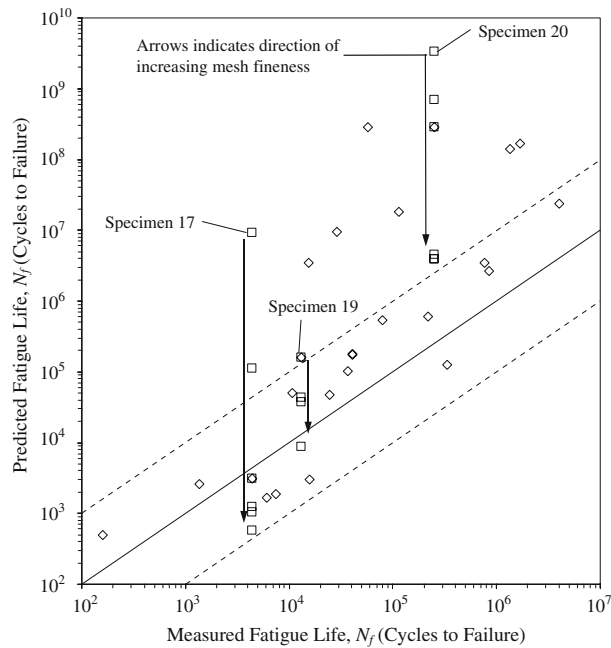
Fig. 7—Comparison between measured and predicted fatigue lives of specimens with additional runs made for specimen 19 at three finer grids, and at two coarser and three finer finite element mesh grids for specimens 17 and 20.

with the smallest predicted number of cycles to failure is located on the surface of the specimen. In the following, the fatigue life prediction for a specimen is always taken as the shortest life resulting at any node in the fe-safe calculations.

The measured and predicted fatigue lives for all 25 porous specimens are compared in Figure 7. A line of perfect correspondence is provided in the figure, to help determine whether a prediction is conservative (below the line) or nonconservative (above the line). It can be seen that 18 of the predicted fatigue lives are within a factor of 10 of the test results, which can be regarded as good agreement. Of these, only five are conservative. Seven data points are in poor agreement with the measurements (*i.e.*, by more than a factor of 10) and are nonconservative, and two of these have predicted lives that are approximately three orders of magnitude longer than the measurements. While these results are generally encouraging, the overall nonconservative nature of the predictions warrants further investigation.

It is well known that fatigue life predictions are very sensitive to local stress concentrations. This issue is of particular importance in the present study, because the simulations rely on pore fractions defined over a volume that is large compared to the microscopic pore geometry. It is unlikely that a node spacing of 0.25 mm resolves the local stress concentrations around small shrinkage pores, which can result in nonconservative fatigue life predictions if the pores are located in a highly stressed region. Therefore, a mesh sensitivity study was performed. Specimen 19 was simulated using three FEA meshes that are finer than the baseline grid (0.25 mm node spacing). The three finer meshes have

node spacings of 0.16, 0.12, and 0.09 mm. Figure 8 shows the predicted stress fields on the surface of specimen 19, for all four meshes. The predicted maximum stress increases from 400 MPa for the baseline mesh to 467, 488, and 602 MPa for the three finer meshes. Note that the applied stress amplitude for specimen 19 is 126 MPa. Obviously, higher maximum stresses result in lower fatigue lives. The predicted fatigue lives for the four meshes are indicated as squares in Figure 7. The fatigue life predictions vary from approximately 160,000 cycles for the coarsest mesh to 8700 for the finest mesh. For specimen 19, the result for the finest mesh is in good agreement with the measured fatigue life of 13,013 cycles to failure. A similar mesh refinement study was performed for specimen 20, where the baseline mesh gives a fatigue life prediction that is three orders of magnitude above the measured life. In addition to the four meshes used for specimen 19, simulations were also performed with two meshes that are coarser than the baseline mesh (node spacings of 0.42 and 0.58 mm). The predicted fatigue lives for specimen 20, shown in Figure 7 as squares, strongly decrease with increasing mesh fineness. The coarsest mesh yields a fatigue life prediction of approximately 3.4×10^9 cycles to failure. The three finest meshes give approximately the same fatigue life, indicating that the predictions converge to a constant value for a sufficiently fine mesh. However, the converged value of approximately 4×10^6 cycles to failure does not agree well with the measured life of 250,000 cycles for specimen 20. This disagreement may be related to the limited sensitivity of the film radiographs from which the porosity field was reconstructed, as is investigated in more detail in Section IV. Because the resolution of the radiography was approximately 100 μm, a node spacing that is smaller than this value does not change or improve the fatigue life predictions.

Mesh refinement studies conducted for other specimens (such as shown in Figure 7 for specimen 17) showed the same trend. Generally, for those specimens for which the prediction for a coarse mesh is already close to the measurement, further mesh refinement does not decrease the predicted fatigue life substantially. For those specimens for which the baseline prediction is vastly nonconservative (*e.g.*, specimen 20), the mesh refinement has a much stronger effect. These differences can be attributed to the nature of the porosity distribution in the specimens. Computational meshes with node spacing on the order of 100 μm are generally not practical in the structural analysis of entire metal castings. Even for the relatively small specimens of the present study, such a fine mesh pushes the limits of current computational capabilities. Furthermore, it appears from the mesh refinement study for specimen 20 that porosity features smaller than 100 μm can play an important role in the fatigue behavior of the specimens. Therefore, in the following, an approximate simulation method is devised that reduces the strong mesh dependence of the results shown in Figure 7 and predicts the measured fatigue lives more closely, even for a relatively coarse mesh.
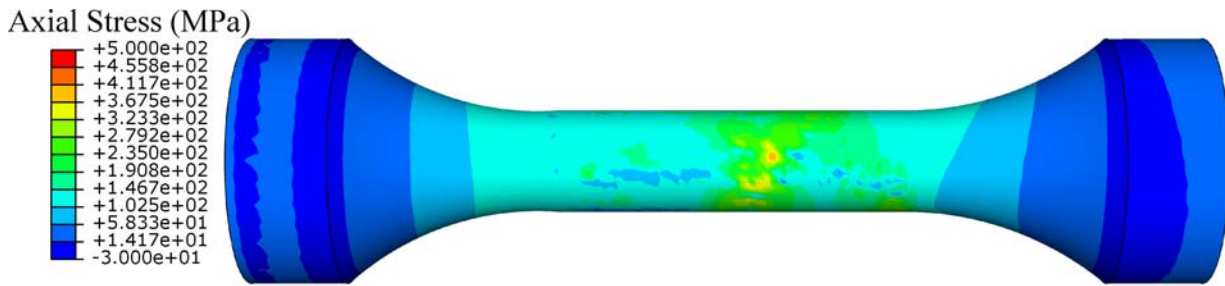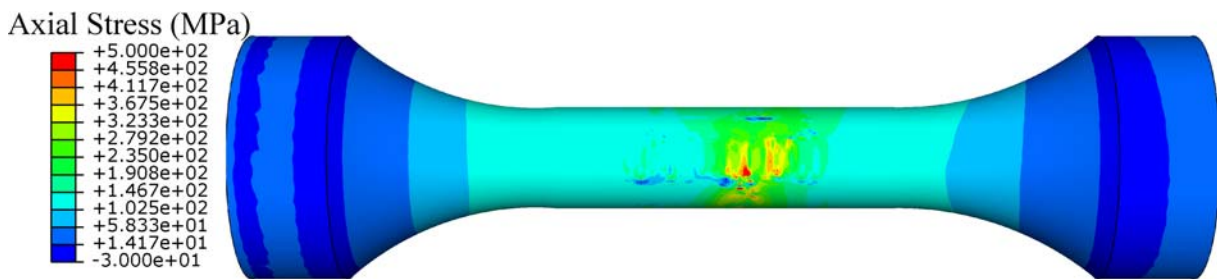
(a) node spacing of 0.25 mm; maximum predicted axial stress is 400 MPa.
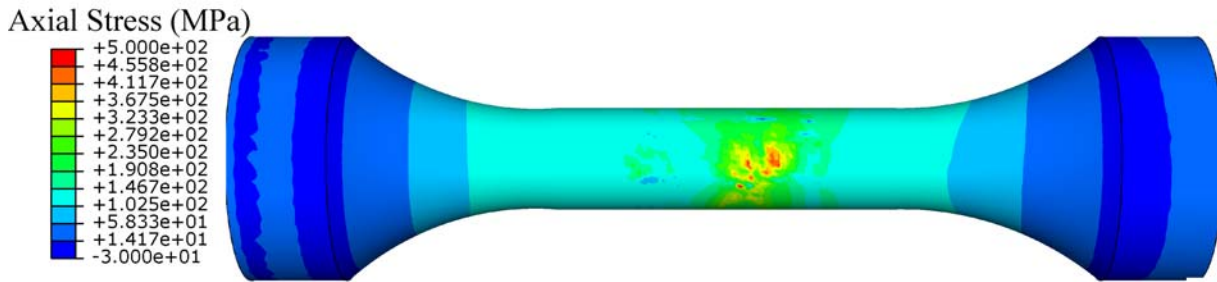
(b) node spacing of 0.16 mm; maximum predicted axial stress is 467 MPa.
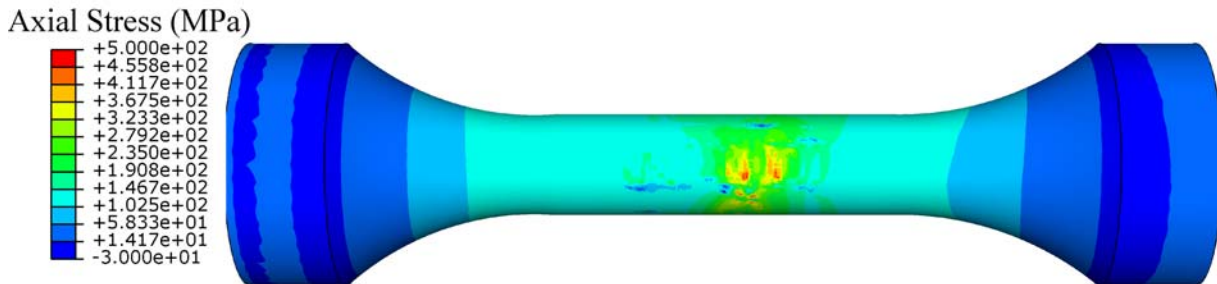
(c) node spacing of 0.12 mm; maximum predicted axial stress is 488 MPa.

(d) node spacing of 0.09 mm; maximum predicted axial stress is 602 MPa.

Fig. 8—Predicted axial stress distribution on surface for four grids used to predict the fatigue life of specimen 19 shown in Fig. 7. Finer grids give higher stresses from more detailed porosity field.

IV. ADAPTIVE SUBGRID MODEL FOR FATIGUE LIFE PREDICTION

The adaptive subgrid model developed in the present study is based on the idea of using a local fatigue notch factor at each node in the fatigue life calculations. This notch factor is intended to account for the effect of porosity that is not at all or only partially resolved in the simulations. The lack of resolution can stem from either a finite element mesh that is too coarse or a porosity that is too small to be detected by standard film radiography (such porosity is referred to as microporosity in the discussion that follows). The use of a local fatigue notch factor is different from the common practice of applying the same notch factor to an entire part or the entire

surface of a part.[3,13] In the present model, a fatigue notch factor is only applied at those locations of the part at which the stress concentrations due to porosity are not fully resolved. The magnitude of the fatigue notch factor is calculated as a function of the local node spacing and the local pore size. If the node spacing is small enough that the stress concentration around a pore of a certain size is fully resolved, the local fatigue notch factor would be equal to unity. If the pore is so small relative to the node spacing that the FEA does not predict any stress concentration, the local fatigue notch factor would be equal to some maximum value that corresponds to that pore. This aspect is what makes the present subgrid model adaptive. The development of the adaptive subgrid model involves numerous considerations that are discussed separately in Sections A through E.

A. Fatigue Notch Factor

A fatigue notch factor, K_f, is commonly used in fatigue life calculations to account for the effects of notches or discontinuities.[3] The fatigue notch factor relates the local notch root stress and strain amplitudes to the nominal true stress and strain amplitudes through a relationship known as Neuber's rule; i.e.,

$$\frac{\Delta \varepsilon}{2} \frac{\Delta \sigma}{2} = K_f^2 \frac{\Delta e}{2} \frac{\Delta S}{2} \qquad [6]$$

where $\Delta \sigma / 2$ and $\Delta \varepsilon / 2$ are the local axial stress and strain amplitudes at the notch root, respectively, and $\Delta S / 2$ and $\Delta e / 2$ are the nominal true stress and strain amplitudes, respectively. The multiaxial version of Neuber's rule uses the stresses and strains in the critical plane, as explained previously in connection with the Brown–Miller algorithm. Equation [6] is solved together with the cyclic stress-strain curve for the notch stress and strain amplitudes; i.e.,

$$\frac{\Delta \varepsilon}{2} = \frac{\Delta \sigma}{2E} + \left(\frac{\Delta \sigma}{2K'}\right)^{\frac{1}{n'}} \qquad [7]$$

The notch strain amplitude resulting from the simultaneous solution of Eqs. [6] and [7] is then used in the strain-life equation (i.e., Eq. [5]) to calculate the fatigue life. The fatigue notch factor, K_f, in Eq. [6] is obtained from[3]

$$K_f = 1 + \frac{K_t - 1}{1 + a/r} \qquad [8]$$

where K_t is the stress concentration factor and r is the notch root radius in millimeters. The material constant a is obtained from the following relation originally developed for wrought steel:[44]

$$a = 0.0254 \cdot \left(\frac{2070}{S_u}\right)^{1.8} \qquad [9]$$

where S_u is the ultimate strength in MPa (Table II). For $r \gg a$, which for $S_u = 1144$ MPa is approximately the case for $r > 1$ mm, Eq. [8] yields that $K_f = K_t$ and the material is said to be fully notch sensitive.[3]

The use of the fatigue notch factor concept outlined here in a strain-life calculation results in accurate predictions of the effect of microporosity on fatigue of cast steel.[19] In Reference 19, additional fatigue tests are presented with cast steel specimens that have only microporosity. Microporosity is generally thought of as porosity that is not detected in standard film radiography. In the context of the present measurements, it is defined as porosity with a pore volume fraction less than approximately 1 pct and with pore radii no larger than approximately 100 μm. Such microporosity should be opposed to the macroporosity in the present specimens (Table I). In the microporosity fatigue life calculations of Reference 19, the notch root radius, r, was taken equal to the radius of the pore, R_p, found on the fracture surface to be responsible for failure, i.e., $r = R_p$. The stress concentration factor, K_t, was taken as a first approximation to be equal to 2.045, which is the value corresponding to a single spherical hole in an essentially infinite body.[45]

Because the fatigue notch factor model discussed here was found to work well for microporosity, it forms the basis for the present subgrid model. As is shown in Section IV–B, pores with a radius less than 100 μm are not at all resolved for finite element node spacings greater than approximately 0.2 mm (in fact, node spacings less than 10 μm would be necessary to correctly calculate the stress concentration for a 100-μm radius pore). For such pores and meshes, the full fatigue notch factor as given by Eq. [8] should thus be applied in the fatigue life calculations. For fully unresolved pores, as in the limiting case of microporosity, the simulations can then be expected to yield the correct fatigue life.

B. Adaptive Stress Concentration Factor

As discussed in Section A, when performing a finite element stress analysis, and the mesh is so coarse relative to the pore size that the predicted stresses are not affected by the presence of the pore (as would be expected for microporosity), the stresses at the location of the pore should be enhanced by a factor that gives the correct stress concentration corresponding to the pore. This factor is referred to as a stress concentration factor, K_t, and values for holes of various shapes and sizes can be found in handbooks (e.g., Reference 45). However, if the node spacing is of the same order as or smaller than the pore size, a finite element stress analysis would predict some or all of the enhanced stresses due to the presence of the pore. In that case, the factor used to enhance the stresses should be less than the full stress concentration factor from a handbook or even equal to unity. Thus, the objective of this section is to determine a relation for an adaptive stress concentration factor, $K_{t,a}$, that is a function of the node spacing, L_n, relative to the pore size. For simplicity, pores are approximated as single spherical holes of a certain effective radius, R_p, in an essentially infinite body, so that the maximum value for $K_{t,a}$ is equal to 2.045.[45]

A finite element elastic stress analysis was performed of a single spherical hole with $R_p = 0.1$ mm inside of a 5-mm-diameter axially loaded cylinder made of 8630

steel. This cylinder diameter is large enough that the predicted stresses around the hole are not influenced by the boundaries. The hole is modeled as a spherical field of nodes having 100 pct porosity ($\phi = 1$); the hole is *not* modeled as a feature in the finite element mesh. The elastic properties at each node are calculated from Eqs. [3] and [4], such that the elastic modulus, E, is essentially equal to zero at the nodes corresponding to the hole. The applied load on the cylinder ends is taken to be 207.4 MPa. Because $K_t = 2.045$ for a single spherical hole,[45] the maximum stress at the hole should be equal to 424 MPa. Figure 9 shows the predicted stress fields at a midsection cut of the hole for three different node spacings: 0.025, 0.1, and 0.2 mm. For the smallest node spacing, the stresses around the hole are well resolved and the predicted maximum stress is equal to 411 MPa. This stress is very close to the handbook

value of 424 MPa, so that $K_{t,a} \approx 1$. For the intermediate node spacing, the hole is poorly resolved and the maximum stress from the FEA is equal to only 264 MPa. Hence, the corresponding adaptive stress concentration factor is $K_{t,a} = 424/264 = 1.606$. For the coarsest mesh, only a single node is present within the hole and the predicted maximum stress from the FEA of 219 MPa is close to the nominal applied stress of 207.4 MPa; therefore, $K_{t,a} = 424/219 = 1.94$.

These results can be generalized by realizing that, for a single hole in an infinite body, the full stress concentration factor is independent of the radius of the hole. Figure 10 shows the computed adaptive stress concentration factor, $K_{t,a}$, as a function of the node spacing to the pore radius ratio, L_n/R_p. It was verified that the same result is obtained for hole radii other than 0.1 mm. It can be seen from Figure 10 that, for $L_n/R_p < 0.08$, the adaptive stress concentration factor is equal to unity, implying that the stresses around the hole are fully resolved. For $L_n/R_p > 4$, the mesh is so coarse that the full stress concentration factor of 2.045 must be applied. For use in the present simulations, the following curve was fit through the computed data points

$$K_{t,a} = 2.045 + (1 - 2.045) \exp\left[\frac{0.08 - L_n/R_p}{1.286}\right] \quad [10]$$

for $L_n/R_p > 0.08$. Equation [10] then provides the stress concentration factor for use in Eq. [8]. For discontinuities other than a single spherical hole, a value that is different from 2.045 could be used in Eq. [10]. Because the use of $K_t = 2.045$ yields accurate fatigue life predictions for the microporosity specimens in Reference 19, this value is kept here.

C. *Implementation in fe-safe*

The software *fe-safe* only allows for the application of a constant fatigue notch factor to the entire surface of

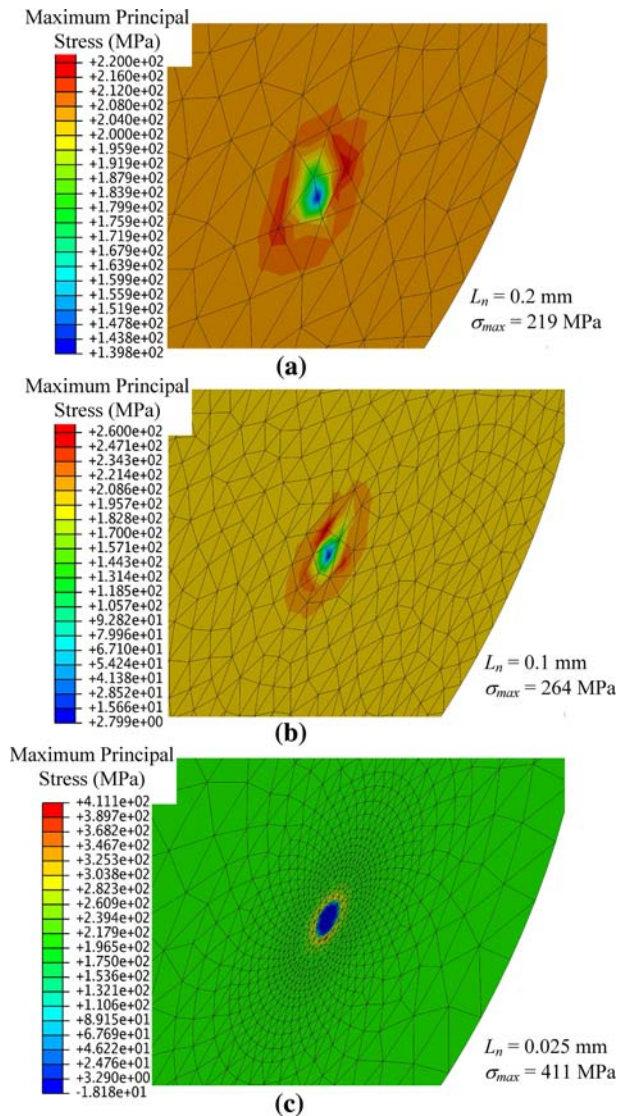Fig. 9—Predicted maximum principal stress distribution for a 100 μm radius spherical hole in a 5 mm diameter cylinder under a loading of 207 MPa, with increasing mesh fineness from (*a*) through (*c*). Node spacing and maximum stress for each case provided.
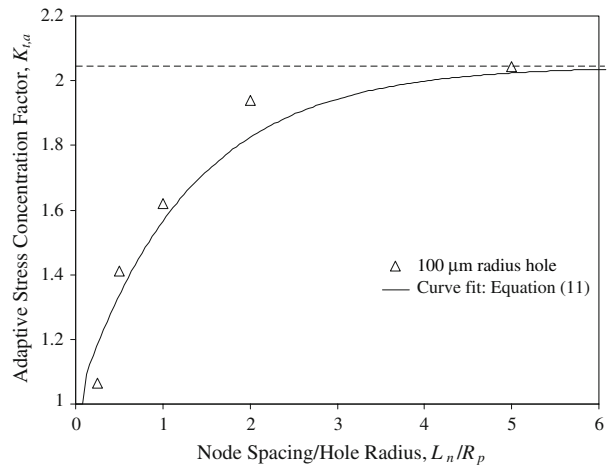
Fig. 10—Adaptive stress concentration factor $K_{t,a}$ required to achieve correct fatigue life at five node spacing to hole radius ratios for a 100 μm radius spherical hole modeled using a porosity field.
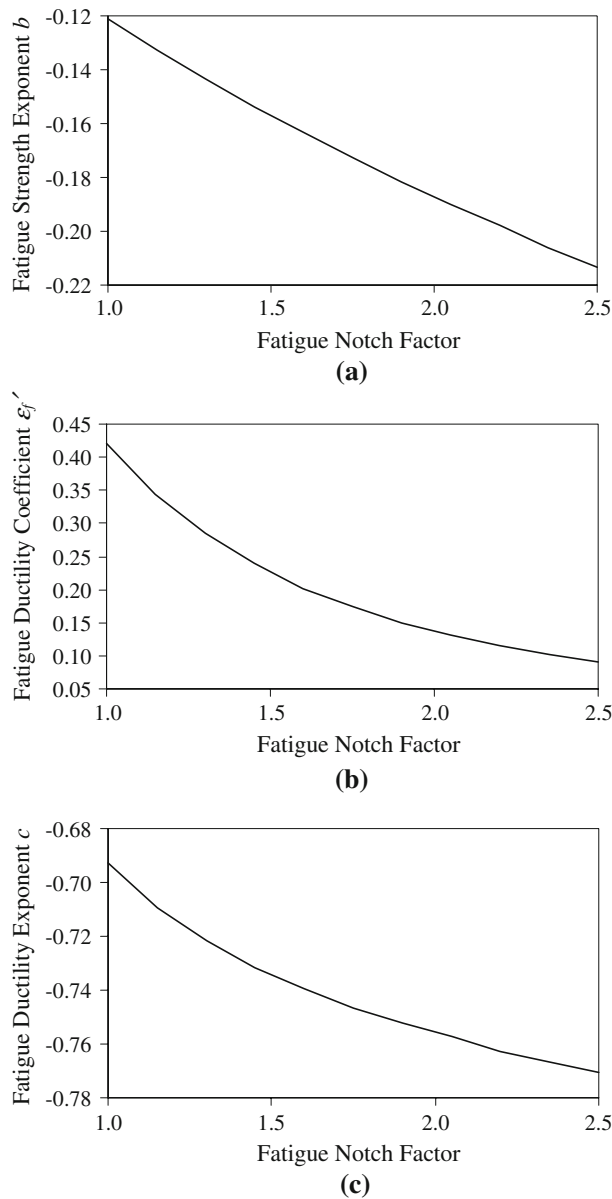
(a)

(b)

(c)

Fig. 11—Fatigue properties as functions of notch factor for (*a*) fatigue strength exponent *b*, (*b*) fatigue ductility coefficient ε_f', and (*c*) fatigue ductility exponent *c*.

the part or the entire part. However, the use of the present adaptive subgrid model necessitates the use of a fatigue notch factor that varies from node to node. This issue can be resolved by making use of the fact that fe-safe allows for temperature dependent fatigue properties (σ_f', ε_f', b, and c) in the strain-life equation, Eq. [5]. That feature is utilized in the present implementation of the adaptive subgrid model, by importing the calculated fatigue notch factors at each node as a temperature field into *fe-safe*, and evaluating the fatigue properties as a function of the fatigue notch factor. The functional dependence between the fatigue properties and the fatigue notch factor must be such that the strain-life equation gives the same life with the modified (K_f dependent) fatigue properties as with the true fatigue

properties but the strains being the notch strains from Neuber's rule, Eq. [6].

To determine the fatigue properties as functions of K_f, software was developed that minimizes the error between a strain-life curve generated for a given K_f value and the true fatigue properties from Table III, and a strain-life curve with $K_f = 1$ but modified fatigue properties. For a given K_f, the fatigue properties σ_f', ε_f', b and c are iterated upon and solved for until the two strain-life curves match. The resulting dependencies of ε_f', b, and c on K_f are plotted in Figures 11(a), (b), and (c), respectively. The present minimization procedure revealed that σ_f' should not be made a function of K_f (and thus be kept at the true value given in Table III).

D. *Pore Size Model*

The sole remaining unknown in the adaptive subgrid model is the pore radius, R_p. It is needed in Eq. [8] for the fatigue notch factor and in Eq. [10] for the adaptive stress concentration factor. Porosity is always characterized by a distribution of pore sizes, rather than a single pore radius, in the volume element over which the porosity volume fraction is defined (*e.g.*, References 27 through 29). For the purpose of fatigue life calculations it is important to know the radius of the largest pore in the distribution, because it is that pore that initiates failure.[19,24,27–29,34] Thus, the present pore size model is concerned primarily with predicting the maximum pore radius, $R_{p,\max}$. In order to keep the model relatively simple, the maximum pore radius is assumed to be dependent on the pore volume fraction, ϕ, only. As explained here, results from both a probabilistic model of pore growth and merging and from experimental measurements are used to develop the pore size model.

The following example illustrates the importance of distinguishing between the mean and maximum pore radii. In Reference 19, the present authors and co-workers performed image analysis on polished metallographic sections of 8630 cast steel specimens having microporosity. The average pore volume fraction was found to be $\phi = 0.7$ pct, and the mean distance between the pores, L_p, was observed to range from 177 to 344 μm. The pore number density, n (*i.e.*, the number of pores per unit volume) can then be estimated from the relation $n = L_p^{-3}$ to be between 2.4×10^{10} and 1.8×10^{11} pores/m^3. Assuming the pores are spherical and have a uniform radius, the pore volume fraction is given by

$$\phi = n \frac{4\pi}{3} R_p^3 \qquad [11]$$

Using these values for ϕ and n, a mean pore radius of $R_p = 21$ to 41 μm is obtained from Eq. [11], which was verified by the image analysis. However, images of the fracture surface of the microporosity specimens revealed that failure always initiated from much larger, isolated pores with a radius on the order of 100 μm.[19] This value corresponds to the radius of the largest pore.

Taking $R_p = 100 \mu m$ and n as estimated earlier, Eq. [11] yields pore volume fractions, ϕ, ranging from 10 to 75 pct, which is clearly unrealistic. Thus, Eq. [11] is not valid for the maximum pore radius.

As part of the present study, a probabilistic pore size distribution model was developed to better understand the phenomena of pore growth and merging and the relationship between the maximum and mean pore radii. Due to space limitations, it is only briefly described here. The pores are assumed to nucleate instantaneously with a certain initial volume fraction and number density and a lognormal size distribution. Based on the microporosity measurements mentioned earlier, the shape of the initial size distribution is adjusted such that for $\phi = 0.7$ pct and $n = 9.97 \times 10^{10} m^{-3}$, the mean pore radius, R_p, is equal to 26 μm and the maximum pore radius, $R_{p,max}$, in the distribution is 100 μm. Each pore in the distribution is assumed to grow at a rate proportional to the square of its radius. In addition, a pore merging model is implemented. Pores are assumed to be capable of merging if their radius exceeds half of the mean spacing between the pores. The frequency of pore merging is determined by the probability that two pores will take part in a merging event. This probability is dependent on the product of the number density ratios of the merging pores (either within a bin of a single pore size meeting the merging criterion or between two bins of different pore sizes). The number density ratio is the number density of one pore size bin divided by the total number density of pores. Merged pores continue to form and grow along with the distribution. Due to merging, the total number density of pores continually decreases as the mean pore radius and total porosity volume fraction increase.

Representative calculated pore size distributions are shown in Figure 12. In Figure 12(a), the curve corresponding to $\phi = 0.1$ pct represents the initial pore size distribution. With an increasing pore fraction, the maximum of the distribution shifts to higher pore radii and the distribution becomes narrower. At approximately $\phi = 3$ pct, significant pore merging is starting to occur. This can be seen in Figure 12(a) by the area under the distribution decreasing and, hence, the total pore number density decreasing. In addition, the pore size distributions develop a tail at pore radii that are much larger than the mean. This can be better seen in Figure 12(b), where the predicted pore size distribution for $\phi = 10$ pct is shown in a log-log plot. At 10 pct, the total number density, mean pore radius, and maximum pore radius are approximately given by $n = 1.17 \times 10^6 m^{-3}$, $R_p = 0.73$ mm, and $R_{p,max} = 2.61$ mm, respectively. The maximum pore radius is difficult to determine from the distribution because of its long tail, but for $\phi = 10$ pct, the value of 2.61 mm corresponds to the mean of the merged pores (Figure 12(b)). This maximum pore radius agrees with the measurements of ASTM radiographs for shrinkage porosity in steel castings presented in Reference 46.

For use in the present adaptive subgrid model, the maximum pore radius results from the probabilistic pore size distribution model were fit to the following piecewise function:
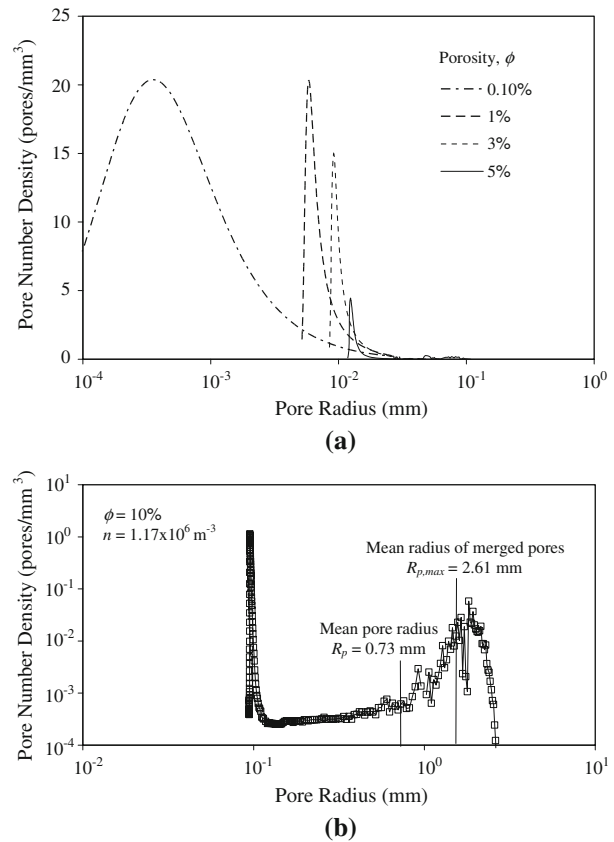

(a)

(b)

Fig. 12—(a) Pore number density distributions at the start of porosity formation (0.1 pct) and at 1, 3, and 5 pct porosity. Number density decreases as pores grow and merge together into larger pores. (b) Pore number density distribution at 10 pct porosity, with mean of merged pores indicated.

$$R_{p,max} = \frac{2825.2 \cdot \phi}{1.0 + 25,846.63 \cdot \phi - 275,154.35 \cdot \phi^2}$$
$$\text{for } \phi \leq 0.0386$$

$$R_{p,max} = 1.76888 - 1.66246 \cdot \exp\left(-21,223.91 \cdot \phi^{3.98865}\right)$$
$$\text{for } 0.0386 < \phi < 0.0941$$

$$R_{p,max} = 3.563 + 0.8877 \cdot \ln(\phi) \quad \text{for } \phi \geq 0.0941 \quad [12]$$

where $R_{p,max}$ is in mm. For ϕ greater than approximately 10 pct, the probabilistic pore size model breaks down, and the last expression given in Eq. [12] represents an extrapolation that is intended to yield realistic maximum pore radii for large pore fractions. The present adaptive subgrid model becomes insensitive to the pore radius for large radii, which, depending on the finite element mesh used, is approximately the case for $R_p > 1$ mm; thus, the accuracy of this extrapolation is not important. The maximum pore radius function is plotted in Figure 13. Superimposed on that figure are several metallographic sections from the present specimens. Good qualitative agreement can be observed between the maximum pore radii calculated from Eq. [12] and the size of the largest pores visible on the sections. Because the present adaptive subgrid model has many other uncertainties and is only intended to
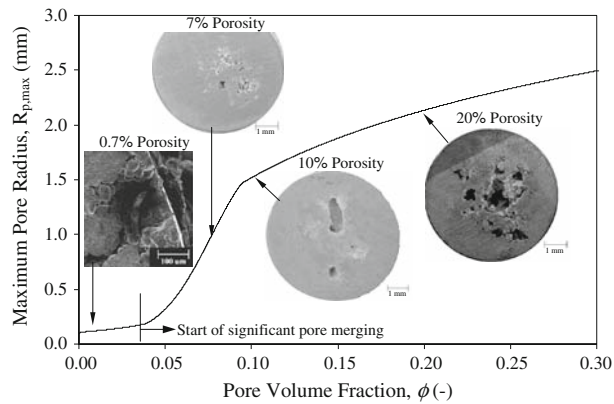
Fig. 13—Relationship for maximum pore size *vs* volume fraction compared with observed porosity in specimens (5 mm diameter).
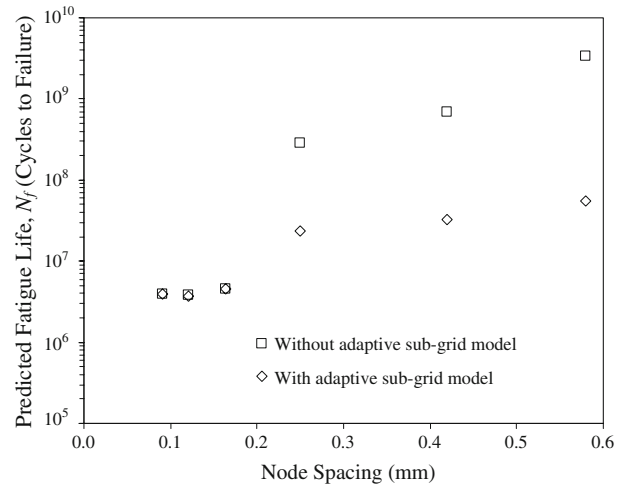

Fig. 14—Effect of finite element model node spacing on predicted fatigue life from fe-safe for specimen 20. Original method without subgrid fatigue model and with subgrid model with $K_{f,max} = 2.045$.

provide a first-order correction to the strong mesh dependence of the fatigue life simulations, the maximum pore radius model can be considered sufficiently accurate. In summary, the function for $R_{p,max}$ given here is used for both the notch root radius, r, in Eq. [8] for the fatigue notch factor, and the pore radius, R_p, in Eq. [10] for the adaptive stress concentration factor.

E. *Results Using the Adaptive Subgrid Model*

The adaptive subgrid fatigue life model is first tested for specimen 20. As previously shown in Figure 7, the original fatigue life predictions for specimen 20, without the subgrid model, are highly dependent on the node spacing. A comparison of those results with the corresponding predictions in which the adaptive subgrid model is employed in the simulations is shown in Figure 14. For the three finest meshes (0.16, 0.12, and 0.09 mm node spacing), the fatigue life predictions are the same with and without the subgrid model; furthermore, the results are independent of the node spacing and can thus be considered converged. The converged value for the predicted fatigue life is ~4 × 10⁶ cycles to failure. The agreement illustrates that the present adaptive subgrid model correctly reduces to a standard stress/fatigue life simulation for a sufficiently fine finite element mesh. In other words, the introduction of the fatigue notch factor in the adaptive subgrid model does not reduce the predicted fatigue life to a value below the one for a fully resolved FEA calculation. For the three coarser meshes (0.25, 0.42, and 0.58 mm node spacing), the fatigue life predictions are substantially above the converged result of approximately 4 × 10⁶ cycles to failure. However, the fatigue lives obtained with the adaptive subgrid model are consistently closer to the converged value and are more mesh independent. For the coarsest mesh, the adaptive subgrid model has the strongest beneficial effect and reduces the fatigue life predicted without the subgrid model by almost two orders of magnitude. While these results for specimen 20 are encouraging and indicate that the adaptive subgrid model is working as intended, it can be seen from Figure 14 that, for the three coarser meshes, the fatigue

lives predicted with the subgrid model are still up to 1 order of magnitude larger than the converged value. This finding suggests that a larger maximum stress concentration factor in Eq. [10], instead of the 2.045 value, would produce even better results. While that is certainly true, the use of a larger maximum stress concentration factor in the adaptive subgrid model is not desirable, because the value of 2.045 gave accurate fatigue life predictions for the microporosity specimens in Reference 19. Furthermore, note that even the finest mesh results are still considerably above the measured fatigue life for specimen 20 (~250,000 cycles to failure (Table I)); thus, factors other than the mesh resolution are causing disagreement between the measured and predicted fatigue lives.

Figure 15 shows the effect of the adaptive subgrid model on the fatigue life predictions for all 25 specimens. These simulations were performed with a node spacing of 0.25 mm. The vertical lines are used to indicate in the figure the movement of the predictions due to the use of the subgrid model. Relative to the measurements, the predictions are much improved, especially for the highly nonconservative data points. It is interesting that those predictions that were already close to the measurements are not affected by the subgrid model and the good agreement remains. This is especially true for the lower lived specimens with fatigue lives of less than ~10,000 cycles to failure. For those specimens, failure is controlled by large porosity features and the stress field is already adequately resolved with a node spacing of 0.25 mm.

Although the adaptive subgrid model results in a considerable improvement in the fatigue life predictions, there are still six data points in Figure 15 for which the prediction is more than an order of magnitude above the measurement. This could be the result of the porosity field not being sufficiently resolved in the X-ray tomography. In particular, the radiography does not detect microporosity, because the resolution is limited by the radiographic film sensitivity to 100 μm, as mentioned
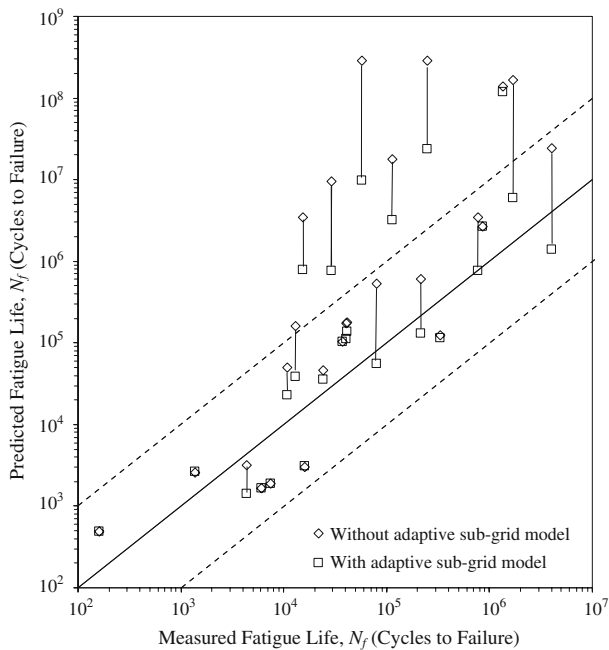
Fig. 15—Comparison between measured and predicted fatigue lives of specimens for node spacing ≈ 0.25 mm for original method (no K_f) and for the subgrid fatigue model with $K_{f,\max} = 2.045$. Prediction uses Abaqus simulated stress field and subgrid fatigue model with fatigue properties dependent on K_f, as shown in Fig. 11. Multiaxial Brown–Miller algorithm with Morrow mean stress correction is used in fe-safe.

Fig. 16—Comparison between measured and predicted fatigue lives of specimens for node spacing ≈ 0.25 mm for the subgrid fatigue model with $K_{f,\max} = 2.045$ (higher values), and the same model but using a uniform background pore size of 100 μm radius (even at nodes at which tomography gives material as 100 pct sound).

earlier. Microporosity was always observed on metallographic sections, such as those shown in Figure 2, in regions next to larger pores. This can be important in a fatigue life calculation, because high stress concentrations occur next to large pores. In order to investigate the sensitivity of the predictions to the presence of microporosity, simulations were performed with a uniform "background" microporosity having a maximum pore radius, $R_{p,\max}$, of 100 μm. This is easily accomplished in the present subgrid model by modifying the pore size model, Eq. [12], such that all values of $R_{p,\max}$ that are less than 100 μm are overwritten with 100 μm (which only occurs for ϕ less than 0.1 pct). The porosity field used in the finite element stress analysis of the specimens was not changed, because microporosity corresponds to very small pore fractions with a negligible effect on the elastic properties.

The effect of the background microporosity on the fatigue life predictions for all 25 specimens is shown in Figure 16. The simulation results in this figure were obtained using the adaptive subgrid model and a node spacing of 0.25 mm. Here, the vertical lines indicate the movement of the predictions due to the addition of the background microporosity. As expected, the addition of the background microporosity lowers the fatigue life predictions for all specimens. However, the magnitude of the effect is not the same for all specimens. For some specimens, background microporosity has a negligible effect, while for others, the predicted fatigue life changes by almost two orders of magnitude. These differences can be attributed to the nature of the porosity field in
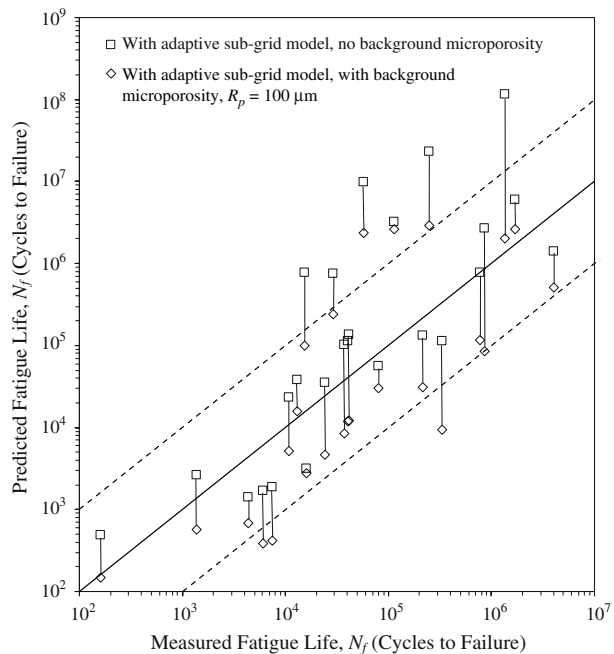
the specimens and the resulting stress redistributions. Overall, with the addition of the background microporosity in the simulations, the agreement between the measured and predicted fatigue lives can now be considered satisfactory.

V. CONCLUSIONS

A simulation method is developed for predicting the effect of shrinkage porosity on the fatigue life of steel castings. The method is validated using previously measured fatigue life data for 25 cast steel test specimens containing up to 21 pct porosity in the gage section.[19] The simulation method relies on the knowledge of the three-dimensional porosity field. In the present study, the porosity field is obtained from X-ray tomography with a resolution of approximately 100 μm.[1] After importing the porosity field into the FEA software, an elastic stress analysis of the fatigue tests is conducted via the method developed in Reference 1. Using this method, the local elastic properties are reduced according to the volume fraction of porosity present at an FEA node. The computed stresses are imported into fatigue analysis software to calculate the fatigue life distribution in the specimens using the strain-life equation for sound steel. It is found that the measured fatigue lives of several of the specimens tested are vastly overpredicted when a finite element mesh is used that is too coarse to resolve all of the porosity-induced local stress concentrations. For this reason, an adaptive subgrid model is developed that employs a local fatigue notch factor to approximately account for

the effect of under-resolved porosity. In this subgrid model, an adaptive stress concentration factor is calculated that depends on the size of a shrinkage pore relative to the node spacing of the finite element mesh. The maximum pore radius is obtained from a probabilistic pore size distribution model as a function of the local pore volume fraction. With the adaptive subgrid model and uniform background microporosity with a maximum pore radius of 100 μm, the measured and predicted fatigue lives are found to be in good overall agreement, even for a relatively coarse FEA mesh. The present simulation method is sufficiently general and flexible that it can be used for the fatigue analysis of complex-shaped steel castings containing porosity. For such production steel castings, X-ray tomographic reconstructions of the three-dimensional porosity field are generally not available. It is anticipated that the porosity field can instead be predicted using advanced casting simulation software.[47,48] A preliminary case study demonstrating such an integrated simulation methodology was presented in Reference 2.

ACKNOWLEDGMENTS

REFERENCES

1. R.A. Hardin and C. Beckermann: *Metall. Mater. Trans. A*, 2007, vol. 38A, pp. 2992–3006.
2. R.A. Hardin, R.K. Huff, and C. Beckermann: in *Modeling of Casting, Welding and Advanced Solidification Processes XI*, C. Gandin and M. Bellet, eds., TMS, Warrendale, PA, 2006, pp. 653–60.
3. R.I. Stephens, A. Fatemi, R.R. Stephens, and H.O. Fuchs: *Metal Fatigue in Engineering*, 2nd ed., Wiley-Interscience, New York, NY, 2000.
4. *2002 Annual Book of ASTM Standards*, ASTM, West Conshohocken, PA, 2002, vol. 03.01, pp. 569–83.
5. S.S. Manson: *Behavior of Materials under Conditions of Thermal Stress*, NACA TN2933, National Advisory Committee for Aeronautics, Washington, DC, 1954.
6. L.F. Coffin: *Trans. ASME*, 1954, vol. 76, pp. 931–50.
7. D.F. Socie and G.B. Marquis: *Multiaxial Fatigue*, Society of Automotive Engineers, Warrendale, PA, 2000.
8. B.-R. You and S.-B. Lee: *Int. J. Fatigue*, 1996, vol. 18 (4), pp. 235–44.
9. C.-C. Chu: *Int. J. Fatigue*, 1996, vol. 19 (Suppl. 1), pp. S325–S330.
10. D. Taylor, P. Bologna, and K. Bel Knani: *Int. J. Fatigue*, 2000, vol. 22, pp. 735–42.
11. Y. Liu, B. Stratman, and S. Mahadevan: *Int. J. Fatigue*, 2006, vol. 28, pp. 747–56.
12. Y. Liu, B. Stratman, and S. Mahadevan: *Rel. Eng. Sys. Saf.*, 2008, vol. 93, pp. 456–67.
13. *fe-safe User Manual*, Safe Technology, Ltd., Sheffield, UK, 2006, pp. 233–39.
14. P.C. Paris and F. Erdogan: *Trans. ASME, J. Basic Eng.*, 1963, vol. D85, pp. 528–34.
15. S.C. Haldimann-Sturm and A. Nussbaumer: *Int. J. Fatigue*, 2008, vol. 30, pp. 528–37.
16. P. Baicchi, L. Collini, and E. Riva: *Eng. Fract. Mech.*, 2007, vol. 74, pp. 539–48.
17. Y. Nadot and V. Denier: *Eng. Fail. Anal.*, 2004, vol. 11, pp. 485–99.
18. P. Hausild, C. Berdin, P. Bompard, and N. Verdiere: *Proc. 6th World 2000 Duplex Conf.*, Associazione Italiana di Metallurgia, Venice, Italy, 2000, pp. 209–18.
19. K.M. Sigl, R. Hardin, R.I. Stephens, and C. Beckermann: *Int. J. Cast Met. Res.*, 2004, vol. 17 (3), pp. 130–46.
20. S. Jayet-Gendrot, P. Gilles, and C. Migne: *Fatigue and Fracture: 1997 PVP-Vol. 350*, 1997, ASME, vol. 1, pp. 107–16.
21. M. Kohno and M. Makioka: *AFS Trans.*, 1970, vol. 78, pp. 9–16.
22. K. Chijiwa, T. Nakayama, and M. Imamura: *35e CIF*, vol. 36, pp. 1–12.
23. P. Heuler, C. Berger, and J. Motz: *Fatigue Fract. Eng. Mater. Struct.*, 1992, vol. 16, pp. 115–36.
24. T. Billaideau, Y. Nadot, and G. Bezine: *Acta Mater.*, 2004, vol. 52, pp. 3911–20.
25. Y. Nadot, J. Mendez, and N. Ranganathan: *Int. J. Fatigue*, 2004, vol. 26, pp. 311–19.
26. T. Mansson and F. Nilsson: *Int. J. Cast Met. Res.*, 2001, vol. 13 (6), pp. 373–78.
27. X. Zhu, J.Z. Yi, J.W. Jones, and J.E. Allison: *Metall. Mater. Trans. A*, 2007, vol. 38A, pp. 1111–22.
28. X. Zhu, J.Z. Yi, J.W. Jones, and J.E. Allison: *Metall. Mater. Trans. A*, 2007, vol. 38A, pp. 1123–35.
29. J. Linder, M. Axelsson, and H. Nilsson: *Int. J. Fatigue*, 2006, vol. 28, pp. 1752–58.
30. D.L. McDowell, K. Gall, M.F. Horstemeyer, and J. Fan: *Eng. Fract. Mech.*, 2003, vol. 70 (1), pp. 49–80.
31. C. Sonsino and J. Ziese: *Int. J. Fatigue*, 1993, vol. 15, pp. 75–84.
32. A. Dabayeh and T.H. Topper: *Fatigue Fract. Eng. Mater. Struct.*, 2000, vol. 23, pp. 993–1006.
33. J.-Y. Buffière, S. Savelli, P.H. Jouneau, E. Maire, and R. Fougères: *Mater. Sci. Eng., A*, 2001, vol. 316, pp. 115–26.
34. Q.G. Wang and P.E. Jones: *Metall. Mater. Trans. B*, 2007, vol. 38B, pp. 615–21.
35. Q.G. Wang, D. Apelian, and D.A. Lados: *J. Light Met.*, 2001, vol. 1, pp. 73–84.
36. B. Skallerud, T. Iveland, and G. Härkegård: *Eng. Fract. Mech.*, 1993, vol. 44 (6), pp. 857–74.
37. Y. Murakami: *Metal Fatigue: Effects of Small Defects and Nonmetallic Inclusions*, Elsevier Science, Ltd., Oxford, United Kingdom, 2002.
38. Y. Xue, C.L. Burton, M.F. Horstmeyer, D.L. McDowell, and J.T. Berry: *Metall. Mater. Trans. B*, 2007, vol. 38B, pp. 601–06.
39. A.C. Kak and M. Slaney: *Principles of Computerized Tomographic Imaging*, Society for Industrial and Applied Mathematics, Philadelphia, PA, 2001, pp. 275–96.
40. R.I. Stephens: *Fatigue and Fracture Toughness of Five Carbon or Low Alloy Cast Steels at Room or Low Climatic Temperatures*, Steel Founders' Society of America, Des Plaines, IL, 1982.
41. *IMSL Fortran Subroutines for Mathematical Applications: Math/Library Volumes 1 and 2*, Visual Numerics, Inc., Houston, TX, 1997.
42. A.P. Roberts and E.J. Garboczi: *J. Am. Ceram. Soc.*, 2000, vol. 83 (12), pp. 3041–48.
43. *Abaqus/Standard*, Abaqus, Inc., Providence, RI, 2006.
44. *Fatigue Design Handbook*, Society of Automotive Engineers, Warrendale, PA, 1968, vol. 4, p. 29.
45. R.E. Peterson: *Stress Concentration Factors*, Wiley-Interscience, New York, NY, 1974, p. 137.
46. K.D. Carlson, S. Ou, R.A. Hardin, and C. Beckermann: *Int. J. Cast Met. Res.*, 2001, vol. 14, pp. 169–83.
47. K.D. Carlson, Z. Lin, R.A. Hardin, C. Beckermann, G. Mazurkevich, and M.C. Schneider: in *Modeling of Casting, Welding and Advanced Solidification Processes X*, D.M. Stefanescu, J.A. Warren, M.R. Jolly, and M.J.M. Krane, eds., TMS, Warrendale, PA, 2003, pp. 295–302.
48. K.D. Carlson, Z. Lin, and C. Beckermann: *Metall. Mater. Trans. B*, 2007, vol. 38B, pp. 541–555.